bioRxiv preprint doi: https://doi.org/10.1101/266759; this version posted February 16, 2018. The copyright holder for this preprint (which was not certified by peer review) is the author/funder. All rights reserved. No reuse allowed without permission.

Control of flagellum length by a grow-and-lock model

Eloïse Bertiaux[1,3], Benjamin Morga[1,2,3], Thierry Blisnick[1], Brice Rotureau[1] & Philippe Bastin[1,4,] *

[1]Trypanosome Cell Biology Unit, Institut Pasteur & INSERM U1201, 25, rue du Docteur Roux, 75015 Paris, France.

[2] Present address: Laboratoire de Génétique et Pathologie des Mollusques Marins, Station de La Tremblade - Ronce Les Bains - 17390 La Tremblade, France

[3] Equal contribution

[4] Lead contact

* Correspondence: pbastin@pasteur.fr

bioRxiv preprint doi: https://doi.org/10.1101/266759; this version posted February 16, 2018. The copyright holder for this preprint (which was not certified by peer review) is the author/funder. All rights reserved. No reuse allowed without permission.

SUMMARY

Several cell types such as photoreceptors and spermatozoa possess very stable cilia and flagella, a feature also encountered in numerous protists. We tested an original model for the control of flagellum length in such cells, using *Trypanosoma brucei* as an experimental system. The grow-and-lock model proposes that the flagellum elongates at a linear rate and that a locking event takes place in a timely defined manner preventing further elongation or shortening. The model implies that modulation of (1) the growth rate or of (2) the timing of the locking event should impact on flagellum length, and (3) that a mature flagellum should display unique characteristics. Here, we provide experimental evidence supporting each of these three postulates. First, reducing the frequency of intraflagellar transport, the machinery responsible for construction, slows down the growth rate and results in the construction of much shorter flagella. Second, we show that the locking event is initiated at a defined stage of the cell cycle and subsequently leads to inhibition of elongation. Third, flagellum maturation is associated to a molecular marker termed FLAM8. Altogether, these results provide support for the grow-and-lock model as a new paradigm for the control of organelle length.

Keywords: cilia and flagella; ciliogenesis; organelle length; microtubules; intraflagellar transport; trypanosome; photoreceptor; spermatozoa

bioRxiv preprint doi: https://doi.org/10.1101/266759; this version posted February 16, 2018. The copyright holder for this preprint (which was not certified by peer review) is the author/funder. All rights reserved. No reuse allowed without permission.

INTRODUCTION

Cilia and flagella (interchangeable terms) are present at the surface of many eukaryotic cells from protists to humans where they are involved in a range of functions including motility, sensing or morphogenesis. Multiple types of ciliary organisations are encountered from one species to another, and also between different cells in the same organism. Striking variations have been noted in cilia composition, positioning or length, presumably reflecting an optimisation related to the function in a given cell type. The lifespan of cilia is also highly variable, from the transitory existence of some primary cilia to the very stable cilia or flagella of photoreceptors or spermatozoa that show little or no turnover of their microtubules.

Despite extensive variation, each cilium or flagellum exhibits a defined length, a process that has fascinated scientists for decades [1]. To decipher the mechanisms that control length, it is essential to understand how the organelle is constructed. Tubulin is delivered via Intraflagellar Transport (IFT) to the distal end of growing microtubules where incorporation takes place [2-4]. Absence of IFT prevents cilium construction in all organisms investigated so far [5]. The control of flagellum length has mostly been studied in the green algae *Chlamydomonas* [6], a member of the Archeoplastida group [7]. In this organism, flagellar microtubules are highly dynamic and exhibit constant disassembly at their plus end. In such a situation, IFT is essential not only for the construction but also for the maintenance of length [8]. Several models have been proposed to explain the control of length in this context, mainly as a balance between assembly and disassembly rates [6], with IFT being a central component [4, 8-11]. These models could function in other systems where cilia display significant microtubule turnover such as in *C. elegans* [12] but could not be applied in cells with more stable cilia.

bioRxiv preprint doi: https://doi.org/10.1101/266759; this version posted February 16, 2018. The copyright holder for this preprint (which was not certified by peer review) is the author/funder. All rights reserved. No reuse allowed without permission.

In mammals, the mouse sperm flagellum relies on IFT for assembly but not for maintenance, and yet the sperm flagellum does not disassemble after maturation [13]. Another case is the connecting cilium of photoreceptors in the retina. These cells display very low turnover [14] and loss of IFT after assembly only impacts ciliary length after 2-3 weeks, possibly because the cell degenerates [15]. How is length control achieved in such conditions? Here, we propose a new model termed grow-and-lock where the organelle grows up to a stage where a signal blocks further elongation or shortening by inducing a modification that locks the structure in a stable (or mature) configuration. The organelle is now ready to perform its final function and does not need length monitoring. In theory, this model is compatible with any type of assembly rate but the easiest situation is to assume a linear growth rate. The moment when the flagellum is locked could be controlled at the level of the flagellum itself but this implies a way to measure length. A simpler option would be to link that event to another cellular process that is timely regulated, such as progression through the cell cycle or through cell differentiation. The locking event would trigger a modification of the organelle that makes its structural elements very stable whereas other components could remain dynamic. This simple model predicts that cells could produce flagella of different lengths by modulating the growth rate and/or the timing of the locking event.

Spermatozoa or photoreceptors do not lend easily to manipulation. By contrast, protists represent great model organisms, are amenable in the laboratory and several of them exhibit very stable flagella. Here, we selected the protist *Trypanosoma brucei* for the investigation of the grow-and-lock model for several reasons. First, its axoneme is very stable [16] and relies on IFT for construction [17, 18] but not for length maintenance [19], exactly like in spermatozoa or photoreceptors. IFT remains active after assembly to maintain other elements but not axoneme composition [19]. Second, when trypanosomes infect mammals or tsetse flies, they progress through several stages of development during which they assemble

bioRxiv preprint doi: https://doi.org/10.1101/266759; this version posted February 16, 2018. The copyright holder for this preprint (which was not certified by peer review) is the author/funder. All rights reserved. No reuse allowed without permission.

flagella of different length [20, 21] and composition [22]. This is reminiscent to what multi-cellular organisms do in different cell types and means that the system is flexible. Third, trypanosomes grow well in culture; they assemble their flagellum in a timely, reproducible and well-characterised manner [23-25]; they are amenable to reverse genetics and IFT has been exhaustively quantified [26].

In this study, we provide experimental evidence that supports each of the major predictions of the grow-and-lock model. The growth rate of the trypanosome flagellar is linear thanks to the continuous recruitment of new IFT trains in the elongating flagellum and its reduction upon IFT kinesin knockdown results in the construction of shorter flagella. The locking event is controlled at the cell cycle level, is triggered prior to cell division and is correlated to the addition of a unique marker protein. Blocking cell division allows for the construction of longer flagella that ultimately mature and reach exactly the same length as the flagellum assembled in the previous generation. The grow-and-lock model provides an opportunity to explain the control of flagellum length in cells with very stable organelles.

bioRxiv preprint doi: https://doi.org/10.1101/266759; this version posted February 16, 2018. The copyright holder for this preprint (which was not certified by peer review) is the author/funder. All rights reserved. No reuse allowed without permission.

RESULTS

IFT delivery remains constant during flagellum construction

The simplest version of the grow-and-lock model can be based on a linear growth rate. This is exactly the case of flagellum assembly in *T. brucei* as measured in culture [24] and during animal infection [27]. This implies a constant delivery of tubulin by IFT no matter the stage of elongation. So far, IFT has only been quantified in mature flagella of *T. brucei* at the procyclic stage maintained in culture [26, 28]. Here, IFT trafficking was examined in the elongating flagellum and compared to the mature flagellum that remains present during the cell cycle, providing an ideal control [23]. This was carried out in live procyclic trypanosomes that express a fusion protein between the fluorescent Tandem Tomato protein (TdT)[29] and the IFT-B protein IFT81, upon endogenous tagging in the *IFT81* locus [30]. In addition to the bright signal at the base, a succession of motile spots was detected all along the length of the flagellum moving in either anterograde or retrograde direction in cells with a single flagellum (Video 1, Fig. 1A1) or in those assembling the new one, hence possessing two flagella (Videos 2-4, Fig. 1 A2-4). At first glance, IFT behaviour looked quite similar in both growing and mature flagella (Fig. 1A). The total amount of fluorescence emitted by the TdT::IFT81 protein was quantified by using the first image of each movie. Plotting the ratio between the total amount of fluorescence in the new flagellum and that in the old one versus the length of the growing flagellum demonstrated a linear correlation between these two parameters (Fig. 1C). This means that when the new flagellum elongates, the total amount of IFT proteins increases. This data suggests that IFT proteins are progressively recruited to the flagellum as it elongates. It also implies that IFT protein concentration in the flagellum is constant at all stages of elongation.

bioRxiv preprint doi: https://doi.org/10.1101/266759; this version posted February 16, 2018. The copyright holder for this preprint (which was not certified by peer review) is the author/funder. All rights reserved. No reuse allowed without permission.

Next, kymograph analysis [26] was carried out to quantify IFT rates and frequencies in cells with one (Fig. 1A1 and Fig. 1B1) or two flagella at different steps of elongation (Fig. 1A2-4 and Fig 1B2-4). Kymograph observations revealed brighter individual tracks for anterograde transport and less intense tracks for retrograde transport as expected [26]. Both IFT speed (Fig. 1D) and frequency (Fig. 1E) were invariant during flagellum elongation, supporting a constant delivery rate of material at the tip of the growing flagellum. We conclude that the IFT delivery rate remains constant during flagellum construction, in agreement with the reported linear growth rate [24, 27].

Knockdown of IFT kinesins reduces frequency and speed of IFT and results in the assembly of short flagella

The grow-and-lock model implies that a modulation of the flagellum growth rate would impact on the final length reached by the organelle. To reduce IFT trafficking, we selected to deplete the expression of kinesin II, the IFT anterograde motor. The genome of *T. brucei* encodes two putative kinesin II proteins (Tb927.5.2090 and Tb927.11.13920) but no kinesin-associated protein (KAP) [31]. Individual RNAi silencing of KIN2A or KIN2B did not result in a visible phenotype: cells assembled apparently normal flagella and grew normally in culture (data not shown), suggesting redundancy. Hence simultaneous knockdown of KIN2A and KIN2B was performed following stable transformation of trypanosomes with a plasmid expressing dsRNA of both *KIN2A* and *KIN2B* under the control of tetracycline-inducible promoters [32]. The efficiency of RNAi silencing in *KIN2A2B*^{RNAi} cells was confirmed by western blotting using an antibody against KIN2B (Fig. S1). The signal for KIN2B dropped by at least 8-fold from day 1 and remained low for at least 6 days, confirming the efficiency of RNAi silencing (Fig. S1). The frequency and speed of IFT was examined upon transformation of *KIN2A2B*^{RNAi} cells with the reporter construct described

bioRxiv preprint doi: https://doi.org/10.1101/266759; this version posted February 16, 2018. The copyright holder for this preprint (which was not certified by peer review) is the author/funder. All rights reserved. No reuse allowed without permission.

above allowing endogenous tagging of IFT81 with TdTomato. Trypanosomes were grown in induced or non-induced conditions and IFT was measured in live uniflagellated cells upon kymograph analysis. In control cells, bright anterograde trains were frequently observed, trafficking from the base to the tip of the flagellum where they were transformed to retrograde trains (Fig. S2A & Video 5). Kymograph analysis revealed that the average anterograde speed was 1.7±0.5 µm.s^{-1} (n=159 trains from 10 separate cells) and the mean frequency was 0.64 train.s^{-1} (Fig. S2B). RNAi-induced cells looked different, the signal at the base of the flagellum appeared brighter and adopted a more elongated shape compared to that in control cells (Fig. S2C). The train frequency was reduced to 0.37.s^{-1} (n=95) after one day of induction, and down to 0.25.s^{-1} after 4 to 6 days in RNAi conditions (n=125)(Video 6). This is visible on the kymograph with fewer traces in induced cells (Fig. S2D) compared to control ones (Fig. S2B). In addition, IFT trains travelled more slowly when kinesin expression was knocked down: 1.4 µm.s^{-1} at days 4 or 6 instead of 1.9 µm.s^{-1} at day 0 (Fig. S2D). We conclude that the joint depletion of KIN2A and KIN2B expression efficiently reduced IFT delivery in the flagellum.

The observed 3-fold reduction in IFT train frequency should result in a significant reduction in the flagellum growth rate that should consequently allow testing the impact of this parameter on the grow-and-lock model. Monitoring the culture by microscopy during the course of RNAi indicated the presence of smaller cells with a shorter flagellum (Fig. 2A). To quantify this reduction, cells were fixed, processed for immunofluorescence assay (IFA) using the axonemal marker Mab25 and DAPI for DNA staining, and the length of the flagellum was measured. Cells that possessed a single flagellum were first examined. In non-induced samples, the length of the axoneme was on average ~20 µm, as expected [23]. However, the length of the flagellum was shorter during the course of RNAi induction, down to ~9 µm at

bioRxiv preprint doi: https://doi.org/10.1101/266759; this version posted February 16, 2018. The copyright holder for this preprint (which was not certified by peer review) is the author/funder. All rights reserved. No reuse allowed without permission.

day 4, yet with a large dispersion (Fig. 2B). Flagellum length remained in that range over the next two days of induction (Fig. 2B), and up to 11 days after having triggered kinesin knockdown (not shown). In control non-induced samples, analysis by scanning electron microscopy revealed the typical elongated trypanosome shape with the flagellum attached to the cell body (Fig. 2C). By contrast, flagellum length was clearly shorter in induced cells that displayed a shorter cell body (Fig. 2D), in agreement with the role of the flagellum in governing trypanosome morphogenesis [17].

The flagellum can be shorter because it is made too short, hence reflecting a defect in construction as predicted by the grow-and-lock model, but it could also be the case because it shortens after construction. To discriminate between these two possibilities, trypanosomes at a late stage of the cell cycle were investigated. These cells can easily be recognised because they possess two nuclei [23]. In control non-induced cells, the length of the new flagellum was ~15 µm whereas that of the old flagellum was ~20 µm (Fig. 3A, grey symbols on Fig. 3B) as expected because construction is not completed before cell division [23, 33]. This was confirmed by scanning electron microscopy of dividing cells: when the cleavage furrow was visible, the length of the new flagellum was shorter than that of the old one (Fig. 3C). In induced *KIN2A2B*^{RNAi} cells, the average length of the new flagellum was around 7 µm, for all induction times examined (Fig. 3A, black symbols on Fig. 3B). Analysis by scanning electron microscopy revealed that the new flagellum is much shorter and that the daughter cell is smaller (Fig. 3D) compared to the non-induced cells (Fig. 3C). This implies that the new flagellum is made too short when the cells are about to divide and supports a major postulate of the "grow and lock model": reducing the growth rate impacts on the length of the flagellum.

bioRxiv preprint doi: https://doi.org/10.1101/266759; this version posted February 16, 2018. The copyright holder for this preprint (which was not certified by peer review) is the author/funder. All rights reserved. No reuse allowed without permission.

The locking event is initiated at a precise time point of the cell cycle

The second postulate of the grow-and-lock model says that a timely controlled event leads to a modification that locks the flagellum and prevents further elongation or shortening. Since flagellum assembly is intimately linked with the progression through the cell cycle in trypanosomes as in other protists [23, 34, 35], we propose that the locking event is controlled by a cell cycle-dependent mechanism rather than at the flagellum level. When a procyclic trypanosome divides, the new flagellum has reached ~80% of the length of the old flagellum meaning that elongation continues up to 20 µm in the daughter cell inheriting that flagellum. Post-division elongation has been experimentally proven but not quantified so far [36] and the events leading to its arrest are unknown. Flagellum growth can stop instantly or could be triggered by a specific signal that would be effective after a lag phase. In the first hypothesis (sharp arrest), flagellum elongation is blocked when the flagellum becomes mature at some point after cell division. In the second hypothesis (delayed arrest), the signal leading to the locking the flagellum could happen prior or after cell division.

Whilst measuring the length of the new flagellum in *KIN2A2B*^{RNAi} cells (7 µm, see above), we noticed that the old flagellum of the same cells was almost twice longer (12 µm, black symbols, Fig. 3B), although it remained shorter than normally expected (20 µm). This could be explained by the first hypothesis if the flagellum keeps on growing slowly after cell division and if the locking event occurs at the expected time. In the second situation, the locking signal is triggered before division and impacts flagellum elongation later on. Therefore, this result does not discriminate between the two hypotheses. To tease apart the mechanism responsible for the locking of the flagellum, cell division was inhibited. If the locking event takes place after division, it should be possible to restore normal flagellum length since flagellum growth should continue unabated. If it is initiated before cell division, it should allow limited growth of the flagellum according to the kinetics of elongation after

bioRxiv preprint doi: https://doi.org/10.1101/266759; this version posted February 16, 2018. The copyright holder for this preprint (which was not certified by peer review) is the author/funder. All rights reserved. No reuse allowed without permission.

activation of the signal. *KIN2A2B*^{RNAi} cells were grown in the presence of 10mM teniposide, a drug that interferes with mitochondrial DNA segregation but neither with basal body duplication nor with flagellum elongation [37]. This resulted in the expected arrest of cell division confirmed on the growth curve (Fig. S3). *KIN2A2B*^{RNAi} cells induced for 5 days were incubated in the presence of 10mM teniposide during 16 or 24 hours (Fig. 4D). After incubation, cells were fixed and processed for IFA with the axonemal marker Mab25 whilst DNA was stained with DAPI. In controls without teniposide, the mitochondrial DNA segregated normally and cells progressed to the typical pattern with 2 kinetoplasts and 2 nuclei preceding cell division (Fig. 4A, top panels). By contrast, kinetoplasts failed to fully segregate in the presence of teniposide (Fig. 4A, bottom panels), inhibiting cell division. In the absence of teniposide, the ratio between the length of the new and the old flagellum in induced *KIN2A2B*^{RNAi} cells was about 60% (Fig. 4B, light grey), in agreement with previous measurements (Fig. 3B). Remarkably, after 16 or 24 hours of incubation with teniposide, the ratio was close to 100%, meaning that the length of the new flagellum had reached the length of the old flagellum at ~12 µm but had failed to reach the normal 20 µm (Fig. 4A, bottom panels & Fig. 4B, dark grey). This implies that the signal for the locking event is triggered prior to cell division and impacts elongation only subsequently.

If this were true, blocking cell division in wild-type cells should result in an increase of the new flagellum from 80 to 100% of the length of the old flagellum but should not lead to further increase of the length. In the absence of teniposide, the ratio between new and old flagella in cells about to divide was close to 80% as expected [25, 33]. After incubation with teniposide, the length of the new flagellum reached that of the old flagellum but did not elongate further (Fig. S4). These experiments demonstrate that a signal is triggered prior to cell division that leads to a subsequent arrest of flagellum elongation.

bioRxiv preprint doi: https://doi.org/10.1101/266759; this version posted February 16, 2018. The copyright holder for this preprint (which was not certified by peer review) is the author/funder. All rights reserved. No reuse allowed without permission.

A molecular marker to monitor flagellum maturation

The last element of the grow-and-lock model implies that a modification of the flagellum takes place preventing further elongation. The data above indicate that the arrest is progressive since it is initiated prior to cell division and leads to an elongation arrest only after division. We therefore searched for candidate molecules that accumulate towards the late phase of flagellum elongation and could serve as markers for flagellum maturation. The FLAM8 protein appeared as an attractive candidate. It is a large protein (3,075 amino acids) of unknown function that was discovered in a proteomic study of purified trypanosome flagella [33]. FLAM8 is abundant at the distal tip of mature flagella but detected in very low concentrations at the first stages of flagellum construction. However, its amount increases during elongation to reach 40% of that of the old flagellum just prior cell division [33]. It means that a significant increase must happen after cell division, which is compatible with the findings above.

If FLAM8 is indeed a marker of flagellum maturation, it should accumulate in the new flagellum of teniposide-treated cells. Therefore, cell division was inhibited using teniposide in induced *KIN2A2B*^{RNAi} cells exactly as above. Cells were fixed and stained by IFA with an anti-FLAM8 antibody, the Mab25 antibody as an axonemal marker, and DAPI to label the DNA. When induced *KIN2A2B*^{RNAi} cells were not treated with teniposide, FLAM8 was abundant at the tip of the old flagellum, but was present in very low amounts or below detection level in the new flagellum (Fig. 5A, top panels). By contrast, in cells treated with teniposide for 24 hours, the new flagellum had elongated further and the FLAM8 signal at its tip was much brighter and looked similar to that at the tip of the mature flagellum (Fig 5A, bottom panels). A circular region of interest was defined around the tip of the new and the old flagella and the total amount of fluorescence was quantified. In untreated induced *KIN2A2B*^{RNAi} cells at an advanced step of their cell cycle, the ratio of FLAM8 signal

bioRxiv preprint doi: https://doi.org/10.1101/266759; this version posted February 16, 2018. The copyright holder for this preprint (which was not certified by peer review) is the author/funder. All rights reserved. No reuse allowed without permission.

intensities between the new and the old flagellum was close to 60% (Fig. 5B, light grey). However, for induced cells treated with teniposide (where the new flagellum reached the length of the old flagellum), the FLAM8 ratio increased to 100% (Fig. 5B, dark grey).

We conclude that maturation of the new flagellum is initiated towards the end of the cell cycle and has an impact in the daughter cell after division. When cytokinesis is inhibited, maturation is triggered but because flagellum elongation is slower in induced *KIN2A2B*^{RNAi} cells due to the reduced IFT trafficking, the locking event took place too early, therefore preventing the new flagellum to reach the normal length of 20 µm. These results support the last point of the grow-and-lock model that implied that the mature flagellum should be different in molecular terms from the elongating flagellum.

bioRxiv preprint doi: https://doi.org/10.1101/266759; this version posted February 16, 2018. The copyright holder for this preprint (which was not certified by peer review) is the author/funder. All rights reserved. No reuse allowed without permission.

DISCUSSION

In this paper, we present a series of experiments that provide support to the grow-and-lock model: the flagellum shows a linear growth rate until a signal triggers a modification of the axoneme that blocks further elongation or shortening (Fig. 6A). The flagellum is now ready for its final function and its length is not modified anymore. In such a model, a cell can produce a shorter flagellum either by a slower growth rate (Fig. 6A, red curve) or by an earlier initiation of the locking event (Fig. 6B, red). Conversely, a longer flagellum can be constructed using a faster growth rate (Fig. 6A, green curve) or by delaying the timing of maturation (Fig. 6B, green). One could also consider that both parameters can be shifted together to achieve a different length.

This model is optimal for cilia and flagella that do not disassemble their microtubules after assembly and maturation. Locking the length of the axoneme in a mature state could have significant advantages for cellular functions. Protein turnover costs energy and this would dispense the cell of a potentially costly maintenance process. A maybe more significant advantage may be found in the fact that cilia and flagella are central elements in the morphogenesis of the three cell types discussed here. In trypanosomes, the flagellum is attached along the length of the cell body from the onset of assembly. Some stages even use a flagella connector to position the new flagellum alongside the existing one [38]. The flagellum actually guides cell morphogenesis and defines the axis of cytokinesis [17, 39]. In spermatozoa, the axoneme of the flagellum is fully elongated before the cascade of morphogenetic events leading the emergence of the typical elongated shape of the cell body. These occur in a precise manner and are articulated around the flagellum [13, 40]. In photoreceptors, the large outer segment develops from the cilium [41] and is actually derived from the fusion of ectosomes that originated from it [42]. In all three situations, one could

bioRxiv preprint doi: https://doi.org/10.1101/266759; this version posted February 16, 2018. The copyright holder for this preprint (which was not certified by peer review) is the author/funder. All rights reserved. No reuse allowed without permission.

imagine the requirement of a stable axoneme both to ensure correct morphogenesis and to fulfil specific cell function after complete differentiation.

What could render axoneme microtubules so stable? Several hypotheses can be put forward. First, the addition of a cap at the tip of microtubule doublets could be sufficient to prevent further assembly or disassembly. The identification of the distal tip FLAM8 protein as a marker of maturation goes along this line but it does not necessarily mean that this protein inhibits elongation. So far, a cap structure has not been detected on electron micrographs of *T. brucei* procyclic flagella [43] but the morphology of the axoneme tip looks very different between growing and mature flagella: whilst it looks disorganised in elongating flagella with some microtubule doublets very close to the central pair and others further away and in contact with the membrane, it is nicely and regularly structured in mature ones [44]. A cap at the tip could also protect against the action of the depolymerising kinesin 13 that has been connected to flagellum length control in the related protists *Leishmania major* [45] or *Giardia intestinalis* [46] but whose contribution appears minor in *T. brucei* [47]. A second possibility is the level of some post-translational modifications of tubulin that could alter the dynamics of microtubules. For example, the tip of the growing flagellum contains a large amount of tyrosinated tubulin that is not detected in the mature flagellum [48]. One could imagine that exhaustive detyrosination protects the axoneme from disassembly. By contrast, the totality of trypanosome tubulin being acetylated, a direct role of tubulin acetylation sounds unlikely [49].

Although this has not been reported so far in trypanosomes, the maturation/locking could be reversible in case the organelle needs to be modified, for example during a differentiation process [50]. One could imagine that a structural cap is removed or that post-translational modifications of tubulin are reverted, for example via the action of specific enzymes [51].

bioRxiv preprint doi: https://doi.org/10.1101/266759; this version posted February 16, 2018. The copyright holder for this preprint (which was not certified by peer review) is the author/funder. All rights reserved. No reuse allowed without permission.

According to the grow-and-lock model, modulations of the growth rate or of the timing of maturation should impact on flagellum length. The linear growth rate does not require modulations during assembly but needs a sufficient supply of IFT proteins to ensure a regular increase of IFT trains in the flagellum and maintain a constant delivery rate of tubulin. This is likely given that the amount of IFT proteins in the cell body largely exceeds that in the flagellum [18, 26, 52]. Moreover, the amount of *IFT* gene transcripts increases during flagellum assembly, followed closely by mRNA from genes coding for axonemal proteins [53, 54]. Examination of mouse photoreceptors during differentiation also indicates a significant amount of IFT proteins in the cell body in addition to the cilium [15, 55]. The depletion of the kinesin motors in trypanosomes led to a 3-fold reduction in the IFT train injection and resulted in the formation of shorter flagella, hence supporting the possibility to modulate flagellum length by slowing down the growth rate, as predicted by the model (Fig. 6B).

Here, we have shown that the event leading to the maturation of the flagellum is linked to the cell cycle timing and is triggered prior to trypanosome division. This could also be the case of multiple protists where flagella are assembled during nuclear mitosis whilst maintaining flagella assembled in the previous generation(s) [23, 34, 35, 56]. The signal being activated before cell division, the cell commits to flagellum maturation even if it practically takes place only in the daughter cell. However, it is not directly controlled by cell division, since its inhibition by the teniposide treatment still allows maturation to occur, as well as elongation arrest.

In mammalian cells, cilia are usually assembled after mitosis (or meiosis for spermatozoa) in the so-called G0 phase of the cell cycle. If post-translational modifications are involved, the enzyme in charge could be expressed from this time point to progressively act on microtubules and finally inhibit assembly. Another timing information could come

bioRxiv preprint doi: https://doi.org/10.1101/266759; this version posted February 16, 2018. The copyright holder for this preprint (which was not certified by peer review) is the author/funder. All rights reserved. No reuse allowed without permission.

from the process of cell differentiation. We note that in both spermatozoa and photoreceptors, assembly of the cilium is one of the first steps in morphological differentiation [13, 42]. Alternatively, the timing of maturation could be controlled at the level of the flagellum once it reaches a certain length. This would require that the cells are able to monitor flagellum length. An elegant possibility is called the time-of-flight model whereby a sensing molecule traffics in association with IFT proteins and undergoes some modification in the flagellum. As the flagellum elongates the time spent for a trip increases and the proportion of modified sensor becomes high enough to trigger the locking event. This model has only been tested in *Chlamydomonas* but was not supported by experimental evidence [57]. As said previously, flagellar microtubules are highly dynamic in this organism and investigation of the time-of-flight model in other types of cilia will be interesting. The simple grow-and-lock model could therefore be suitable for different types of cilia and flagella with different options for the control of the growth rate and for both the mode and the timing of maturation of the organelle.

bioRxiv preprint doi: https://doi.org/10.1101/266759; this version posted February 16, 2018. The copyright holder for this preprint (which was not certified by peer review) is the author/funder. All rights reserved. No reuse allowed without permission.

bioRxiv preprint doi: https://doi.org/10.1101/266759; this version posted February 16, 2018. The copyright holder for this preprint (which was not certified by peer review) is the author/funder. All rights reserved. No reuse allowed without permission.

ACKNOWLEDGEMENTS

We acknowledge Derrick Robinson (Bordeaux, France), Paul McKean (Lancaster, UK) and Robert Lee Douglas (Berkeley, USA) for generous gifts of antibodies and Linda Kohl (Paris, France) for critical reading of the manuscript. We are thankful to the Ultrastructural BioImaging Plateforme for providing access to their equipment. E.B. is supported by fellowships from French National Ministry for Research and Technology (doctoral school CDV515) and from La Fondation pour la Recherche Médicale (FRM) (FDT20170436836). B.M. was supported by a Roux post-doctoral fellowship from the Institut Pasteur. This work is funded by ANR grants (11-BSV8-016 and 14-CE35-0009-01), by a French Government Investissement d'Avenir programme, Laboratoire d'Excellence "Integrative Biology of Emerging Infectious Diseases" (ANR-10-LABX-62-IBEID) and by La Fondation pour la Recherche Médicale (Equipe FRM DEQ20150734356). The funders had no role in the study design, data collection and analysis, decision to publish or preparation of the manuscript.

AUTHOR CONTRIBUTIONS

E.B., B.M., B.R. & P.B. conceived and designed the experiments; E.B., B.M. and T.B. performed the experiments; T.B. prepared the figures, E.B. and P.B. wrote the manuscript. All authors commented on the manuscript.

DECLARATION OF INTEREST

The authors declare no competing financial interests.

bioRxiv preprint doi: https://doi.org/10.1101/266759; this version posted February 16, 2018. The copyright holder for this preprint (which was not certified by peer review) is the author/funder. All rights reserved. No reuse allowed without permission.

REFERENCES

1. Broekhuis, J.R., Leong, W.Y., and Jansen, G. (2013). Regulation of cilium length and intraflagellar transport. International review of cell and molecular biology *303*, 101-138.
2. Kozminski, K.G., Johnson, K.A., Forscher, P., and Rosenbaum, J.L. (1993). A motility in the eukaryotic flagellum unrelated to flagellar beating. Proc Natl Acad Sci U S A *90*, 5519-5523.
3. Wren, K.N., Craft, J.M., Tritschler, D., Schauer, A., Patel, D.K., Smith, E.F., Porter, M.E., Kner, P., and Lechtreck, K.F. (2013). A differential cargo-loading model of ciliary length regulation by IFT. Current biology : CB *23*, 2463-2471.
4. Craft, J.M., Harris, J.A., Hyman, S., Kner, P., and Lechtreck, K.F. (2015). Tubulin transport by IFT is upregulated during ciliary growth by a cilium-autonomous mechanism. J Cell Biol *208*, 223-237.
5. Prevo, B., Scholey, J.M., and Peterman, E.J.G. (2017). Intraflagellar transport: mechanisms of motor action, cooperation, and cargo delivery. FEBS J *284*, 2905-2931.
6. Ludington, W.B., Ishikawa, H., Serebrenik, Y.V., Ritter, A., Hernandez-Lopez, R.A., Gunzenhauser, J., Kannegaard, E., and Marshall, W.F. (2015). A systematic comparison of mathematical models for inherent measurement of ciliary length: how a cell can measure length and volume. Biophys J *108*, 1361-1379.
7. Adl, S.M., Simpson, A.G., Lane, C.E., Lukes, J., Bass, D., Bowser, S.S., Brown, M.W., Burki, F., Dunthorn, M., Hampl, V., et al. (2012). The revised classification of eukaryotes. J Eukaryot Microbiol *59*, 429-493.
8. Marshall, W.F., and Rosenbaum, J.L. (2001). Intraflagellar transport balances continuous turnover of outer doublet microtubules: implications for flagellar length control. J Cell Biol *155*, 405-414.
9. Engel, B.D., Ludington, W.B., and Marshall, W.F. (2009). Intraflagellar transport particle size scales inversely with flagellar length: revisiting the balance-point length control model. J Cell Biol *187*, 81-89.
10. Liang, Y., Pang, Y., Wu, Q., Hu, Z., Han, X., Xu, Y., Deng, H., and Pan, J. (2014). FLA8/KIF3B phosphorylation regulates kinesin-II interaction with IFT-B to control IFT entry and turnaround. Developmental cell *30*, 585-597.
11. Chien, A., Shih, S.M., Bower, R., Tritschler, D., Porter, M.E., and Yildiz, A. (2017). Dynamics of the IFT machinery at the ciliary tip. eLife *6*.
12. Hao, L., Thein, M., Brust-Mascher, I., Civelekoglu-Scholey, G., Lu, Y., Acar, S., Prevo, B., Shaham, S., and Scholey, J.M. (2011). Intraflagellar transport delivers tubulin isotypes to sensory cilium middle and distal segments. Nature cell biology *13*, 790-798.
13. San Agustin, J.T., Pazour, G.J., and Witman, G.B. (2015). Intraflagellar transport is essential for mammalian spermiogenesis but is absent in mature sperm. Molecular biology of the cell *26*, 4358-4372.
14. Besharse, J.C., and Hollyfield, J.G. (1979). Turnover of mouse photoreceptor outer segments in constant light and darkness. Invest Ophthalmol Vis Sci *18*, 1019-1024.
15. Jiang, L., Wei, Y., Ronquillo, C.C., Marc, R.E., Yoder, B.K., Frederick, J.M., and Baehr, W. (2015). Heterotrimeric kinesin-2 (KIF3) mediates transition zone and axoneme formation of mouse photoreceptors. J Biol Chem *290*, 12765-12778.

bioRxiv preprint doi: https://doi.org/10.1101/266759; this version posted February 16, 2018. The copyright holder for this preprint (which was not certified by peer review) is the author/funder. All rights reserved. No reuse allowed without permission.

16. Vincensini, L., Blisnick, T., Bertiaux, E., Hutchinson, S., Georgikou, C., Ooi, C.P., and Bastin, P. (2017). Flagellar incorporation of proteins follows at least two different routes in trypanosomes. Biol Cell.
17. Kohl, L., Robinson, D., and Bastin, P. (2003). Novel roles for the flagellum in cell morphogenesis and cytokinesis of trypanosomes. Embo J *22*, 5336-5346.
18. Absalon, S., Blisnick, T., Kohl, L., Toutirais, G., Dore, G., Julkowska, D., Tavenet, A., and Bastin, P. (2008). Intraflagellar transport and functional analysis of genes required for flagellum formation in trypanosomes. Molecular biology of the cell *19*, 929-944.
19. Fort, C., Bonnefoy, S., Kohl, L., and Bastin, P. (2016). Intraflagellar transport is required for the maintenance of the trypanosome flagellum composition but not its length. Journal of cell science *129*, 3026-3041.
20. Rotureau, B., Subota, I., and Bastin, P. (2011). Molecular bases of cytoskeleton plasticity during the Trypanosoma brucei parasite cycle. Cell Microbiol *13*, 705-716.
21. Van Den Abbeele, J., Claes, Y., van Bockstaele, D., Le Ray, D., and Coosemans, M. (1999). Trypanosoma brucei spp. development in the tsetse fly: characterization of the post-mesocyclic stages in the foregut and proboscis. Parasitology *118*, 469-478.
22. Rotureau, B., Subota, I., Buisson, J., and Bastin, P. (2012). A new asymmetric division contributes to the continuous production of infective trypanosomes in the tsetse fly. Development *139*, 1842-1850.
23. Sherwin, T., and Gull, K. (1989). The cell division cycle of Trypanosoma brucei brucei: timing of event markers and cytoskeletal modulations. Philos Trans R Soc Lond B Biol Sci *323*, 573-588.
24. Bastin, P., MacRae, T.H., Francis, S.B., Matthews, K.R., and Gull, K. (1999). Flagellar morphogenesis: protein targeting and assembly in the paraflagellar rod of trypanosomes. Mol Cell Biol *19*, 8191-8200.
25. Robinson, D.R., Sherwin, T., Ploubidou, A., Byard, E.H., and Gull, K. (1995). Microtubule polarity and dynamics in the control of organelle positioning, segregation, and cytokinesis in the trypanosome cell cycle. J Cell Biol *128*, 1163-1172.
26. Buisson, J., Chenouard, N., Lagache, T., Blisnick, T., Olivo-Marin, J.C., and Bastin, P. (2013). Intraflagellar transport proteins cycle between the flagellum and its base. Journal of cell science *126*, 327-338.
27. Tyler, K.M., Matthews, K.R., and Gull, K. (2001). Anisomorphic cell division by African trypanosomes. Protist *152*, 367-378.
28. Huet, D., Blisnick, T., Perrot, S., and Bastin, P. (2014). The GTPase IFT27 is involved in both anterograde and retrograde intraflagellar transport. eLife *3*, e02419.
29. Shaner, N.C., Campbell, R.E., Steinbach, P.A., Giepmans, B.N., Palmer, A.E., and Tsien, R.Y. (2004). Improved monomeric red, orange and yellow fluorescent proteins derived from Discosoma sp. red fluorescent protein. Nature biotechnology *22*, 1567-1572.
30. Bhogaraju, S., Cajanek, L., Fort, C., Blisnick, T., Weber, K., Taschner, M., Mizuno, N., Lamla, S., Bastin, P., Nigg, E.A., et al. (2013). Molecular basis of tubulin transport within the cilium by IFT74 and IFT81. Science *341*, 1009-1012.
31. Julkowska, D., and Bastin, P. (2009). Tools for analyzing intraflagellar transport in trypanosomes. Methods Cell Biol *93*, 59-80.
32. Wang, Z., Morris, J.C., Drew, M.E., and Englund, P.T. (2000). Inhibition of trypanosoma brucei gene expression by RNA interference using an integratable vector with opposing T7 promoters. J Biol Chem *275*, 40174-40179.

bioRxiv preprint doi: https://doi.org/10.1101/266759; this version posted February 16, 2018. The copyright holder for this preprint (which was not certified by peer review) is the author/funder. All rights reserved. No reuse allowed without permission.

33. Subota, I., Julkowska, D., Vincensini, L., Reeg, N., Buisson, J., Blisnick, T., Huet, D., Perrot, S., Santi-Rocca, J., Duchateau, M., et al. (2014). Proteomic analysis of intact flagella of procyclic Trypanosoma brucei cells identifies novel flagellar proteins with unique sub-localization and dynamics. Molecular & cellular proteomics : MCP *13*, 1769-1786.
34. Dawson, S.C., and House, S.A. (2010). Life with eight flagella: flagellar assembly and division in Giardia. Curr Opin Microbiol *13*, 480-490.
35. Noel, C., Gerbod, D., Delgado-Viscogliosi, P., Fast, N.M., Younes, A.B., Chose, O., Roseto, A., Capron, M., and Viscogliosi, E. (2003). Morphogenesis during division and griseofulvin-induced changes of the microtubular cytoskeleton in the parasitic protist, Trichomonas vaginalis. Parasitol Res *89*, 487-494.
36. Farr, H., and Gull, K. (2009). Functional studies of an evolutionarily conserved, cytochrome b5 domain protein reveal a specific role in axonemal organisation and the general phenomenon of post-division axonemal growth in trypanosomes. Cell motility and the cytoskeleton *66*, 24-35.
37. Robinson, D.R., and Gull, K. (1991). Basal body movements as a mechanism for mitochondrial genome segregation in the trypanosome cell cycle. Nature *352*, 731-733.
38. Moreira-Leite, F.F., Sherwin, T., Kohl, L., and Gull, K. (2001). A trypanosome structure involved in transmitting cytoplasmic information during cell division. Science *294*, 610-612.
39. Zhou, Q., Liu, B., Sun, Y., and He, C.Y. (2011). A coiled-coil- and C2-domain-containing protein is required for FAZ assembly and cell morphology in Trypanosoma brucei. Journal of cell science *124*, 3848-3858.
40. Leblond, C.P., and Clermont, Y. (1952). Definition of the stages of the cycle of the seminiferous epithelium in the rat. Ann N Y Acad Sci *55*, 548-573.
41. Molday, R.S., and Moritz, O.L. (2015). Photoreceptors at a glance. Journal of cell science *128*, 4039-4045.
42. Salinas, R.Y., Pearring, J.N., Ding, J.D., Spencer, W.J., Hao, Y., and Arshavsky, V.Y. (2017). Photoreceptor discs form through peripherin-dependent suppression of ciliary ectosome release. J Cell Biol *216*, 1489-1499.
43. Woolley, D., Gadelha, C., and Gull, K. (2006). Evidence for a sliding-resistance at the tip of the trypanosome flagellum. Cell motility and the cytoskeleton *63*, 741-746.
44. Höög, J.L., Lacomble, S., O'Toole, E.T., Hoenger, A., McIntosh, J.R., and Gull, K. (2014). Modes of flagellar assembly in Chlamydomonas reinhardtii and Trypanosoma brucei. eLife *3*, e01479.
45. Blaineau, C., Tessier, M., Dubessay, P., Tasse, L., Crobu, L., Pages, M., and Bastien, P. (2007). A novel microtubule-depolymerizing kinesin involved in length control of a eukaryotic flagellum. Current biology : CB *17*, 778-782.
46. Dawson, S.C., Sagolla, M.S., Mancuso, J.J., Woessner, D.J., House, S.A., Fritz-Laylin, L., and Cande, W.Z. (2007). Kinesin-13 regulates flagellar, interphase, and mitotic microtubule dynamics in Giardia intestinalis. Eukaryotic cell *6*, 2354-2364.
47. Chan, K.Y., and Ersfeld, K. (2010). The role of the Kinesin-13 family protein TbKif13-2 in flagellar length control of Trypanosoma brucei. Mol Biochem Parasitol *174*, 137-140.
48. Sherwin, T., Schneider, A., Sasse, R., Seebeck, T., and Gull, K. (1987). Distinct localization and cell cycle dependence of COOH terminally tyrosinolated alpha-tubulin in the microtubules of Trypanosoma brucei brucei. J Cell Biol *104*, 439-446.

bioRxiv preprint doi: https://doi.org/10.1101/266759; this version posted February 16, 2018. The copyright holder for this preprint (which was not certified by peer review) is the author/funder. All rights reserved. No reuse allowed without permission.

49. Schneider, A., Plessmann, U., and Weber, K. (1997). Subpellicular and flagellar microtubules of Trypanosoma brucei are extensively glutamylated. Journal of cell science *110 (Pt 4)*, 431-437.
50. Ooi, C.P., and Bastin, P. (2013). More than meets the eye: understanding Trypanosoma brucei morphology in the tsetse. Frontiers in cellular and infection microbiology *3*, 1-12.
51. Gadadhar, S., Bodakuntla, S., Natarajan, K., and Janke, C. (2017). The tubulin code at a glance. Journal of cell science *130*, 1347-1353.
52. Franklin, J.B., and Ullu, E. (2010). Biochemical analysis of PIFTC3, the Trypanosoma brucei orthologue of nematode DYF-13, reveals interactions with established and putative intraflagellar transport components. Mol Microbiol *78*, 173-186.
53. Morga, B., and Bastin, P. (2013). Getting to the heart of intraflagellar transport using Trypanosoma and Chlamydomonas models: the strength is in their differences. Cilia *2*, 16.
54. Archer, S.K., Inchaustegui, D., Queiroz, R., and Clayton, C. (2011). The cell cycle regulated transcriptome of Trypanosoma brucei. PloS one *6*, e18425.
55. Pazour, G.J., Baker, S.A., Deane, J.A., Cole, D.G., Dickert, B.L., Rosenbaum, J.L., Witman, G.B., and Besharse, J.C. (2002). The intraflagellar transport protein, IFT88, is essential for vertebrate photoreceptor assembly and maintenance. J Cell Biol *157*, 103-113.
56. Wheeler, R.J., Gluenz, E., and Gull, K. (2011). The cell cycle of Leishmania: morphogenetic events and their implications for parasite biology. Mol Microbiol *79*, 647-662.
57. Ishikawa, H., and Marshall, W.F. (2017). Testing the time-of-flight model for flagellar length sensing. Molecular biology of the cell *28*, 3447-3456.
58. Le Ray, D., Barry, J.D., Easton, C., and Vickerman, K. (1977). First tsetse fly transmission of the "AnTat" serodeme of Trypanosoma brucei. Ann Soc Belg Med Trop *57*, 369-381.
59. Brun, R., and Schonenberger (1979). Cultivation and in vitro cloning or procyclic culture forms of Trypanosoma brucei in a semi-defined medium. Short communication. Acta tropica *36*, 289-292.
60. Wirtz, E., Leal, S., Ochatt, C., and Cross, G.A. (1999). A tightly regulated inducible expression system for conditional gene knock-outs and dominant-negative genetics in Trypanosoma brucei. Mol Biochem Parasitol *99*, 89-101.
61. Redmond, S., Vadivelu, J., and Field, M.C. (2003). RNAit: an automated web-based tool for the selection of RNAi targets in Trypanosoma brucei. Mol Biochem Parasitol *128*, 115-118.
62. Kelly, S., Reed, J., Kramer, S., Ellis, L., Webb, H., Sunter, J., Salje, J., Marinsek, N., Gull, K., Wickstead, B., et al. (2007). Functional genomics in Trypanosoma brucei: a collection of vectors for the expression of tagged proteins from endogenous and ectopic gene loci. Mol Biochem Parasitol *154*, 103-109.
63. Burkard, G., Fragoso, C.M., and Roditi, I. (2007). Highly efficient stable transformation of bloodstream forms of Trypanosoma brucei. Mol Biochem Parasitol *153*, 220-223.
64. Absalon, S., Kohl, L., Branche, C., Blisnick, T., Toutirais, G., Rusconi, F., Cosson, J., Bonhivers, M., Robinson, D., and Bastin, P. (2007). Basal body positioning is controlled by flagellum formation in Trypanosoma brucei. PloS one *2*, e437.
65. Pradel, L.C., Bonhivers, M., Landrein, N., and Robinson, D.R. (2006). NIMA-related kinase TbNRKC is involved in basal body separation in Trypanosoma brucei. Journal of cell science *119*, 1852-1863.

bioRxiv preprint doi: https://doi.org/10.1101/266759; this version posted February 16, 2018. The copyright holder for this preprint (which was not certified by peer review) is the author/funder. All rights reserved. No reuse allowed without permission.

66. Chenouard, N., Buisson, J., Bloch, I., Bastin, P., and Olivo-Marin, J.C. (2010). Curvelet analysis of kymograph for tracking bi-directional particles in flurescence microscopy images. International Conference on Image Processing, in press.
67. Subota, I., Rotureau, B., Blisnick, T., Ngwabyt, S., Durand-Dubief, M., Engstler, M., and Bastin, P. (2011). ALBA proteins are stage regulated during trypanosome development in the tsetse fly and participate in differentiation. Molecular biology of the cell *22*, 4205-4219.

bioRxiv preprint doi: https://doi.org/10.1101/266759; this version posted February 16, 2018. The copyright holder for this preprint (which was not certified by peer review) is the author/funder. All rights reserved. No reuse allowed without permission.

FIGURE LEGENDS

Figure 1. IFT trafficking during flagellum construction is compatible with a linear growth rate

(A) Still images of AnTat1.1E cells expressing a TdTomato::IFT81 from the endogenous locus. Subpanel 1 shows a cell with a single flagellum (Video S1) and subpanels 2-4 show cells at successive stages of flagellum construction (Videos S2-S4). Orange and white arrowheads indicate the new and the old flagellum, respectively. (B) Kymographs extracted from the corresponding videos where the X axis corresponds to flagellum length (horizontal scale bar, 2 μm) and the Y axis represents the elapsed time (vertical bar, 1s). (C) The ratios between the total fluorescence intensity Raw Integrated density in the new and the old flagellum were calculated and plotted according to the length of the new flagellum. A linear correlation curve is indicated together with its R^2 coefficient. (D) The ratio between IFT rates (anterograde transport, blue circles; retrograde transport, red squares) in the new flagellum and the old flagellum from the same cell was calculated and plotted according to the length of the new flagellum. Retrograde transport is more difficult to detect and data were only incorporated when the signal was sufficiently reliable. (E) Quantification of the ratio between the IFT frequency (anterograde transport, blue circles; retrograde transport, red squares) in the new flagellum and the old flagellum in the same cell was calculated and plotted versus the length of the new flagellum. See Table 1 for total number of trains analysed.

Figure 2. Reduction of IFT train frequency impacts on flagellum length in *KIN2A2B*^{RNAi} cells.

(A) IFA of non-induced *KIN2A2B*^{RNAi} cells, or cells induced for 3 or 6 days as indicated, fixed in methanol, and stained with the Mab25 antibody to detect the axoneme (white). The top

bioRxiv preprint doi: https://doi.org/10.1101/266759; this version posted February 16, 2018. The copyright holder for this preprint (which was not certified by peer review) is the author/funder. All rights reserved. No reuse allowed without permission.

panels show the phase-contrast image merged with DAPI (blue) and Mab25 signal (white). Scale bar: 10µm. The bottom panels show Mab25 staining (white) merged with DAPI (blue). (B) Dot plot showing flagellum length during the course of RNAi induction of *KIN2A2B*^{RNAi} cells including 100 uni-flagellated cells for each time point. The mean values are indicated with a bold segment. (C-D) Scanning electron microscopy analysis of non-induced (C) and induced *KIN2A2B*^{RNAi} cells after 6 days (D).

Figure 3. The new flagellum is built shorter upon reduction of IFT train frequency in *KIN2A2B*^{RNAi} cells.

(A) IFA images of non-induced and 6-day induced *KIN2A2B*^{RNAi} cells obtained after methanol fixation and staining with the Mab25 antibody labeling the axoneme (red). The top panels show the phase-contrast images merged with DAPI (white) and the Mab25 axonemal marker (red) and the bottom ones show the Mab25 signal (red) merged with DAPI (white). Scale bar: 10µm. (B) Dot plot showing the length of old and new flagella during the course of RNAi induction of *KIN2A2B*^{RNAi} measured in cells possessing 2 kinetoplasts and 2 nuclei (n= 50 for each time point). (C) Scanning electron microscopy pictures of non-induced (C) and induced *KIN2A2B*^{RNAi} cells after 6 days (D). The purple arrow indicates the cleavage furrow. Orange and white arrowheads show the new and the old flagellum, respectively.

Figure 4. Inhibition of cell division impacts flagellar length.

(A) IFA pictures of 6-day induced *KIN2A2B*^{RNAi} cells that were left untreated (top panels) or treated for 24 hours with teniposide (bottom panels), stained with the Mab25 antibody targeting the axoneme (red) and DAPI labeling DNA (white). The left panels show the phase-contrast image merged with DAPI (white) and Mab25 signal (red). The right panels show the Mab25 signal (red) and DAPI (white). Orange and white arrowheads show the new and the

bioRxiv preprint doi: https://doi.org/10.1101/266759; this version posted February 16, 2018. The copyright holder for this preprint (which was not certified by peer review) is the author/funder. All rights reserved. No reuse allowed without permission.

old flagellum, respectively. The white arrows show the bridge linking the kinetoplasts after treatment with teniposide. Scale bar: 5µm. (B) Ratios between the length of the new flagellum and the old flagellum for 6-day induced *KIN2A2B*^{RNAi} cells treated (dark bars, n=112) or not (white bars, n=163) with teniposide during 24 hours. The results are shown for three independent experiments.

Figure 5. The event leading to flagellum maturation is triggered prior to cell division.

(A) IFA pictures of 6 day-induced *KIN2A2B*^{RNAi} cells non-treated or treated for 24 hours with teniposide, fixed in methanol and stained using the Mab25 antibody to detect the axoneme (red), the anti-FLAM8 (green) and DAPI (blue). The left panels show the phase-contrast image merged with DAPI (blue), the anti-FLAM8 (green) and Mab25 antibody (red). The right panels show the anti-FLAM8 signal only (white). Orange and white arrowheads show the new and the old flagellum, respectively. The white circles are centered on the FLAM8 signal. Scale bar: 5µm. (B) Ratios between the FLAM8 fluorescent signal intensity in the new and the old flagellum in 6 day-induced *KIN2AB*^{RNAi} cells treated (n=109) or not (n=60) with teniposide during 24 hours. Two independent experiments are shown.

Figure 6. The grow-and-lock model to explain the control of flagellum length

(A) The flagellum elongates with a linear growth rate until a point where it is locked (arrow) and shows neither assembly nor disassembly. Keeping the same growth rate but triggering the locking event earlier (red) or later (green) will result in the formation of shorter or longer flagella. (B) A slower (red) or faster (green) growth rate allows the production of shorter or longer flagella without having to change the timing of the locking event.

bioRxiv preprint doi: https://doi.org/10.1101/266759; this version posted February 16, 2018. The copyright holder for this preprint (which was not certified by peer review) is the author/funder. All rights reserved. No reuse allowed without permission.

STAR METHODS

Plasmids, cell lines, and culture conditions

The pleomorphic strain *T. brucei* AnTat1.1E [58] was used for transformation with p2675TdTIFT81. Cells were cultured in SDM79 medium [59] supplemented with hemin, 10% fetal bovine serum and 10mM glycerol. All the other procyclic *T. brucei* cell lines were derivatives of the strain 427 and grown in SDM79 medium with hemin and 10% fetal bovine serum. All the cells were cultivated at 27°C. The 29–13 cell line expressing the T7 RNA polymerase and the tetracycline-repressor has been described previously [60]. For generation of the *KIN2A2B*^{RNAi} cell line, a 489-nucleotide fragment of *KIN2A* (Tb927.11.13920) was amplified by PCR flanked by HindIII and XhoI sites and cloned in the compatible sites of the pZJM vector. The *KIN2B* (Tb 927.5.2090) fragment was generated by chemical synthesis by GeneCust Europe (Dudelange, Luxembourg). Genecust cloned these fragment into the pZJM vector [32], allowing tetracycline-inducible expression of dsRNA generating RNAi upon transfection in the 29-13 recipient cell line. The dsRNA is expressed from two tetracycline-inducible T7 promoters facing each other in the pZJM vector. Primers were selected using the RNAit algorithm to ensure that the fragment lacked significant identity to other genes to avoid cross-RNAi [61]. For generation of the *KIN2A2B*^{RNAi} expressing TdT::IFT81 cell line and AnTat1.1E expressing TdT::IFT81, the first 500 nucleotides of the *IFT81* gene (Gene DB number Tb927.10.2640) were chemically synthesised (GeneCust, Luxembourg) and cloned in frame with the TdTomato gene within the HindIII and ApaI sites of the p2675 vector [62]. The construct was linearised within the *IFT81* sequence with the enzyme XcmI and nucleofected [63] in the *KIN2A2B*^{RNAi} or the AnTat1.1E cell line, leading to integration by homologous recombination in the *IFT81* endogenous locus and to expression of the full-length coding sequence of IFT81 fused to TdTomato. Transfectants were grown in media with

bioRxiv preprint doi: https://doi.org/10.1101/266759; this version posted February 16, 2018. The copyright holder for this preprint (which was not certified by peer review) is the author/funder. All rights reserved. No reuse allowed without permission.

the appropriate antibiotic concentration and clonal populations were obtained by limited dilution.

For inhibition of the cell division, teniposide (Sigma SML0609), a topoisomerase II inhibitor was dissolved in DMSO and added to trypanosome cultures at a final concentration of 200 µM [37] during 24 hours (*KIN2A2B*^{RNAi} strain) and 8 hours (wild-type strain). In the control flask, the same volume of DMSO was added (63 µL).

Scanning electron microscopy

For scanning electron microscopy, samples were fixed overnight at 4°C with 2.5% glutaraldehyde in 0.1 M cacodylate buffer (pH 7.2) and post-fixed in 2% OsO_4 in the same buffer. After serial dehydration, samples were dried at the critical point and coated with platinum according to standard procedures [64]. Observations were made in a JEOL 7600F microscope.

Immunofluorescence and live cell imaging

Cultured parasites were washed twice in SDM79 medium without serum or in Phosphate Buffer Saline (PBS), and spread directly onto poly-L-lysine coated slides. The slides were air-dried for 10 min, fixed in methanol at −20°C for 30 s and rehydrated for 10 min in PBS. For immuno-detection, slides were incubated with primary antibodies diluted in PBS with 0.1% Bovine Serum Albumin (BSA) for 1 h at 37°C. Three washes of 10 min were performed and the secondary antibody diluted in PBS with 0.1% BSA was added to the slides. After an incubation of 45 min at 37°C, slides were washed three times in PBS for 10 min and DAPI (2 µg/µl) was added. Slides were mounted with coverslips using ProLong antifade reagent (Invitrogen). The antibodies used were the Mab25 monoclonal antibody recognising TbSAXO1, a protein found all along the trypanosome axoneme [65], an anti-IFT172 mouse

bioRxiv preprint doi: https://doi.org/10.1101/266759; this version posted February 16, 2018. The copyright holder for this preprint (which was not certified by peer review) is the author/funder. All rights reserved. No reuse allowed without permission.

monoclonal antibody diluted at 1/200 [18], an anti-FLAM8 rabbit polyclonal 1/500 (kind gift of Paul McKean, Lancaster University, UK). Subclass-specific secondary antibodies coupled to Alexa 488 and Cy3 (1/400; Jackson ImmunoResearch Laboratories, West Grove, PA) were used for double labelling. Sample observation was performed using a DMI4000 microscope equipped with a 100X NA 1.4 lens (Leica, Wetzlar, Germany) and images captured with an ORCA-03G Hamamatsu camera. Pictures were analyzed using ImageJ 1.47g13 software (National Institutes of Health, Bethesda, MD) and images were merged and superimposed using Adobe Photoshop CC. For fluorescence quantification, we have used the Raw Integrated Density values and removed the background at all these values. For live video microscopy, cells were covered with a coverslip and observed directly with the DMI4000 microscope at room temperature. Videos were acquired using an Evolve 512 EMCCD Camera (Photometrics, Tucson, AZ), driven by the Metavue acquisition software (Molecular Probes, Sunnyvale, CA). IFT trafficking was recorded at 100 (AnTat1.1E expressing TdT::IFT81) or 250 (*KIN2A2B*^{RNAi} expressing TdT::IFT81) milliseconds per frame during 30 seconds. Kymographs were extracted and analysed as described previously [26, 66].

Western blot analysis

Cells were washed in PBS and boiled in Laemmli loading buffer before SDS-PAGE separation, loading 20 µg of total cell protein per lane. Proteins were transferred overnight at 25V at 4°C to polyvinylidene fluoride membranes (PVDF), then blocked with 5% skimmed milk in PBS-Tween 0.1% (PBST) and incubated with primary antibodies diluted in 1% milk and PBST. The anti-KIN2B (a kind gift of Robert L. Douglas, Berkeley) serum was diluted 1/100. As loading controls, antibodies against ALBA proteins [67] diluted 1/500 were used. Three membrane washes were performed with PBST for 5 minutes. Species-specific secondary antibodies coupled to horseradish peroxidase (GE Healthcare) were diluted

bioRxiv preprint doi: https://doi.org/10.1101/266759; this version posted February 16, 2018. The copyright holder for this preprint (which was not certified by peer review) is the author/funder. All rights reserved. No reuse allowed without permission.

1/20,000 in PBST containing 1% milk and incubated for 1 hour. Final detection was carried out using an enhanced chemoluminescence kit and a high performance chemoluminescence film according to manufacturer's instructions (Amersham, Piscataway, NJ).

bioRxiv preprint doi: https://doi.org/10.1101/266759; this version posted February 16, 2018. The copyright holder for this preprint (which was not certified by peer review) is the author/funder. All rights reserved. No reuse allowed without permission.

SUPPLEMENTAL INFORMATION

Figure S1. RNAi efficiently targets KIN2B at the protein level.

Total protein samples of non-induced and induced *KIN2A2B*^{RNAi} cells were prepared after the indicated number of days. Proteins were separated by SDS-PAGE, transferred to a PVDF membrane that was incubated with the anti-KIN2B (top picture) or the anti-ALBA that detects ALBA3 and ALBA4 as loading control (bottom picture).

Figure S2. The frequency of IFT trains is reduced in *KIN2A2B*^{RNAi} cells.

Live imaging of a non-induced (A) and a 6-day induced *KIN2A2B*^{RNAi} cell (B) expressing the TdT::IFT81 from its endogenous locus. Still images from Video S5 (A) and S6 (B) at the indicated time points showing the movement of IFT trains. White arrowheads indicate the successive position of anterograde IFT trains. Kymograph analyses from non-induced (C) and induced cells (D) show clear anterograde IFT traces that are highlighted in color. Note the difference in frequency between non-induced and induced cells. Horizontal scale bar is 2µm and vertical scale bar is 2s.

Figure S3. Teniposide blocks cell proliferation.

Growth curve of wild-type cells untreated (grey continuous line) or treated with teniposide for 24h (grey dotted line) and 6 day-induced *KIN2A2B*^{RNAi} cells untreated (red continuous line) or treated with teniposide (purple dotted line).

Figure S4. Inhibition of cell division and flagellum growth in wild-type cells

(A) IFA pictures of or wild-type cells that were left untreated (top panels) or treated for 24 hours with teniposide (bottom panels), stained with the Mab25 antibody targeting the

bioRxiv preprint doi: https://doi.org/10.1101/266759; this version posted February 16, 2018. The copyright holder for this preprint (which was not certified by peer review) is the author/funder. All rights reserved. No reuse allowed without permission.

axoneme (red) and DAPI labeling DNA (white). The left panels show the phase-contrast image merged with DAPI (white) and Mab25 signal (red). The right panels show the Mab25 signal (red) and DAPI (white). Orange and white arrowheads show the new and the old flagellum, respectively. The white arrows show the bridge linking the kinetoplasts after treatment with teniposide. Scale bar: 5µm. (B) Ratios between the length of the new flagellum and the old flagellum for wild-type cells treated (dark bars, n=150) or not (white bars, n=180) with teniposide during 8 hours (D). The results are shown for three independent experiments.

Supplementary Videos

Video S1: Visualisation of TdT::IFT81 in AnTat1.1E cells.

TdT::IFT81 is found inside the trypanosome flagellum where it travels by IFT. Live procyclic, wild-type *T. brucei* cell transfected with TdT::IFT81 observed by time-lapse epifluorescence microscopy using a DMI4000 microscope at room temperature. Frames were taken every 100 ms for 30 s by an Evolve 512 EMCCD Camera. Example of a cell with a single flagellum.

Video S2: Visualisation of TdT::IFT81 in AnTat1.1E cells.

Same as Video S1 but example of a cell with two flagella, the new one being at early phase of assembly.

Video S3: Visualisation of TdT::IFT81 in 1.1E cells.

bioRxiv preprint doi: https://doi.org/10.1101/266759; this version posted February 16, 2018. The copyright holder for this preprint (which was not certified by peer review) is the author/funder. All rights reserved. No reuse allowed without permission.

Same as Video S1 but example of a cell with two flagella, the new one being at an intermediate phase of assembly.

Video S4: Visualisation of TdT::IFT81 in AnTat1.1E cells.

Same as Video S1 but example of a cell with two flagella, the new one being at a late phase of assembly.

Video S5: Visualisation of TdT::IFT81 in *KIN2A2B*^{RNAi} cells.

This is an example of a non-induced cell showing robust IFT. IFT proteins are found at the base of the flagellum and as motile trains trafficking both ways in the flagellum.

Video S6: Visualisation of TdT::IFT81 in *KIN2A2B*^{RNAi} cells.

This is an example of a cell induced for 6 days where the frequency of IFT is much reduced whereas the total amount of IFT protein at the base is significantly increased.

bioRxiv preprint doi: https://doi.org/10.1101/266759; this version posted February 16, 2018. The copyright holder for this preprint (which was not certified by peer review) is the author/funder. All rights reserved. No reuse allowed without permission.

Table 1: IFT speed and frequency in growing and mature flagella of AnTat1E cells expressing TdT::IFT81. The number of measured trains is given in parentheses. Since retrograde trains are more difficult to detect, only non-ambiguous ones were used for analysis, hence the reduced number.

		Uniflagellated cells	Biflagellated cells	
			New F	Old F
Speed ($\mu m.sec^{-1}$)	**Anterograde**	1.65 ± 0.36 (329)	1.63 ± 0.40 (396)	1.9 ± 0.53 (419)
	Retrograde	5.09 ± 0.86 (297)	5.29 ± 0.60 (284)	5.38 ± 1.0 (261)
Frequency ($trains.sec^{-1}$)	**Anterograde**	1.13 ± 0.21	1.00 ± 0.22	1.04 ± 0.33
	Retrograde	1.59 ± 0.28	1.78 ± 0.84	1.7 ± 0.63

bioRxiv preprint doi: https://doi.org/10.1101/266759; this version posted February 16, 2018. The copyright holder for this preprint (which was not certified by peer review) is the author/funder. All rights reserved. No reuse allowed without permission.

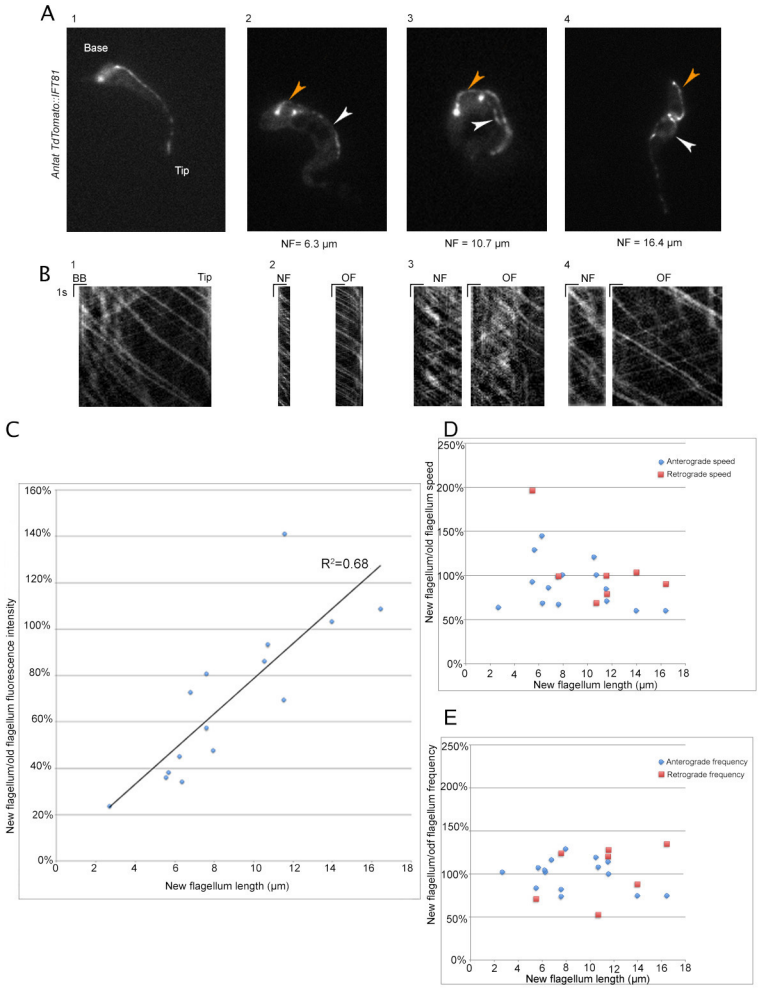

Figure 1

bioRxiv preprint doi: https://doi.org/10.1101/266759; this version posted February 16, 2018. The copyright holder for this preprint (which was not certified by peer review) is the author/funder. All rights reserved. No reuse allowed without permission.

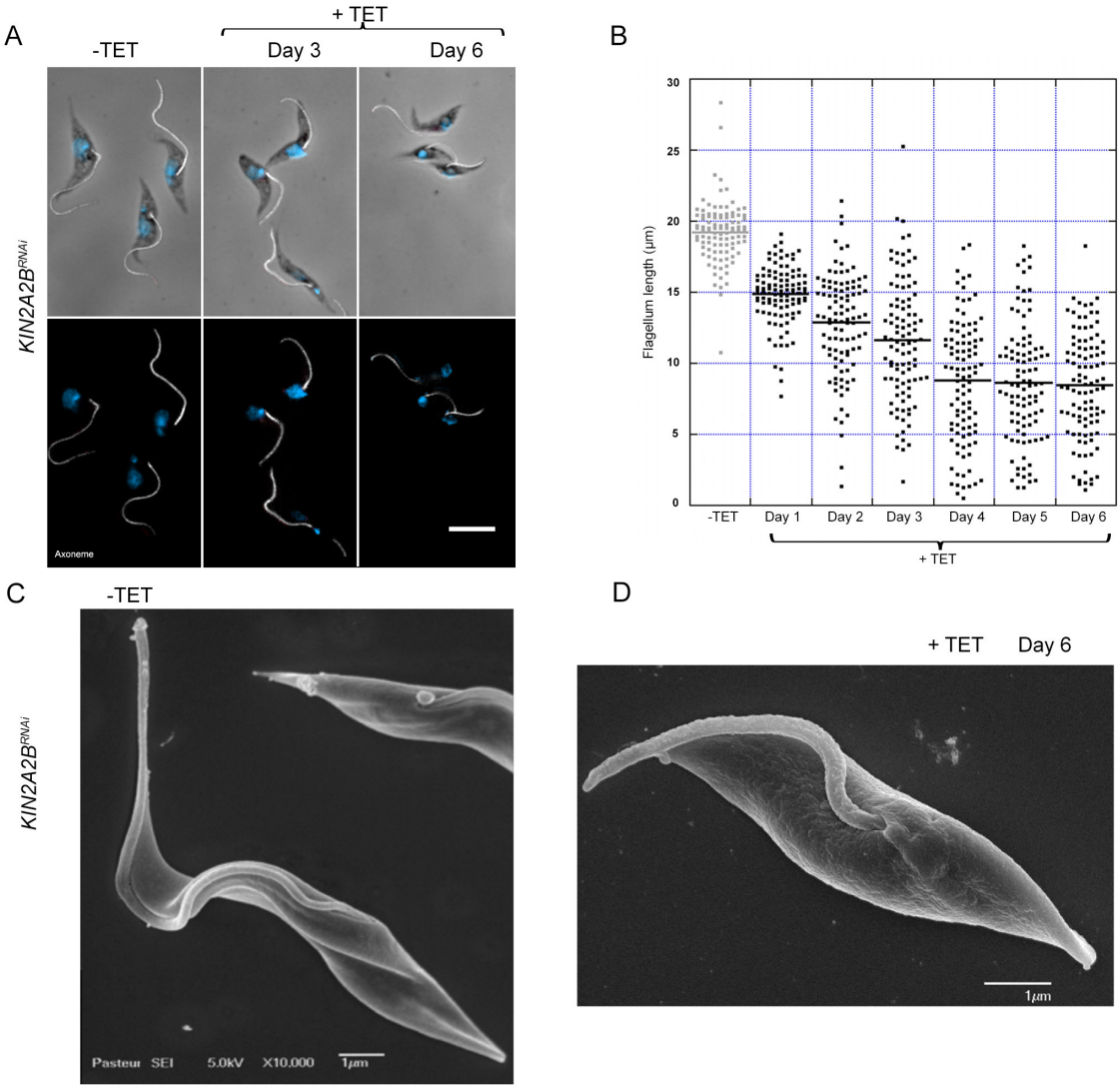

Figure 2

bioRxiv preprint doi: https://doi.org/10.1101/266759; this version posted February 16, 2018. The copyright holder for this preprint (which was not certified by peer review) is the author/funder. All rights reserved. No reuse allowed without permission.

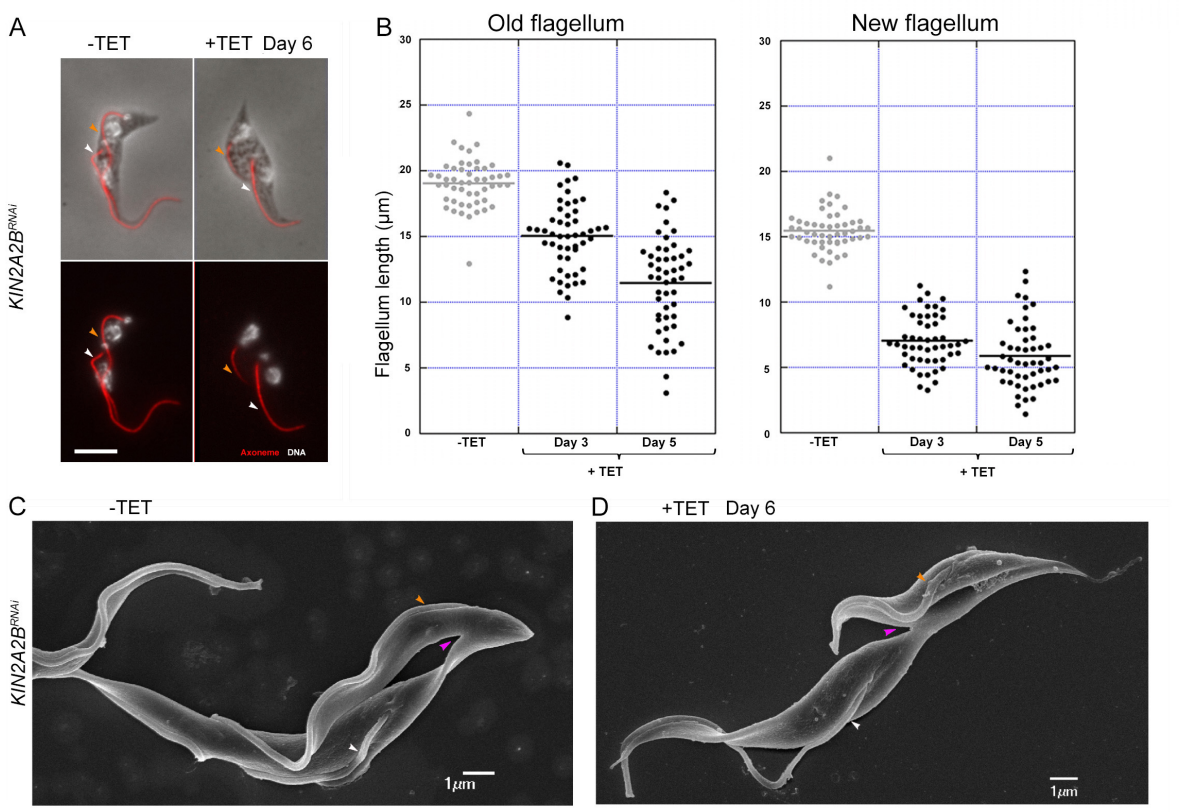

Figure 3

bioRxiv preprint doi: https://doi.org/10.1101/266759; this version posted February 16, 2018. The copyright holder for this preprint (which was not certified by peer review) is the author/funder. All rights reserved. No reuse allowed without permission.

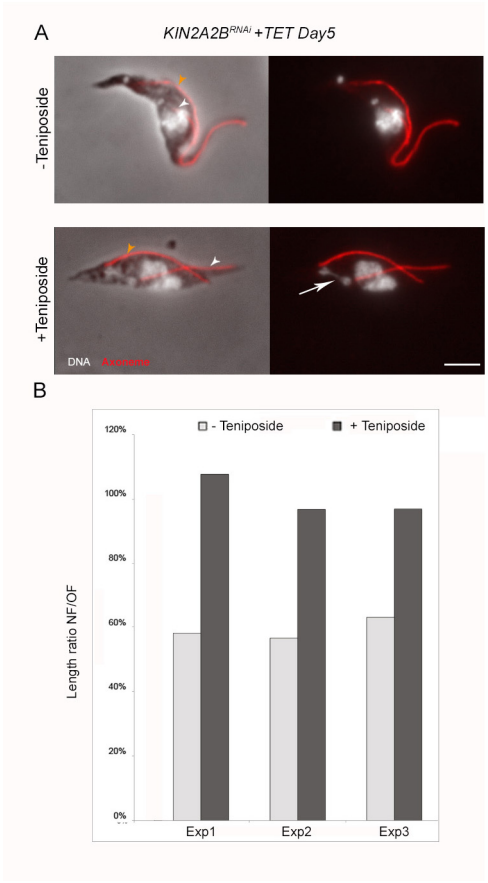

Figure 4

bioRxiv preprint doi: https://doi.org/10.1101/266759; this version posted February 16, 2018. The copyright holder for this preprint (which was not certified by peer review) is the author/funder. All rights reserved. No reuse allowed without permission.

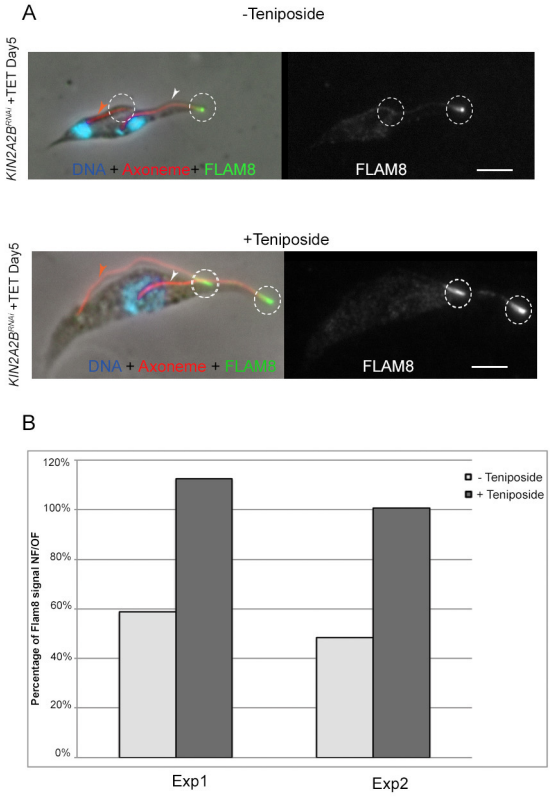

Figure 5

bioRxiv preprint doi: https://doi.org/10.1101/266759; this version posted February 16, 2018. The copyright holder for this preprint (which was not certified by peer review) is the author/funder. All rights reserved. No reuse allowed without permission.

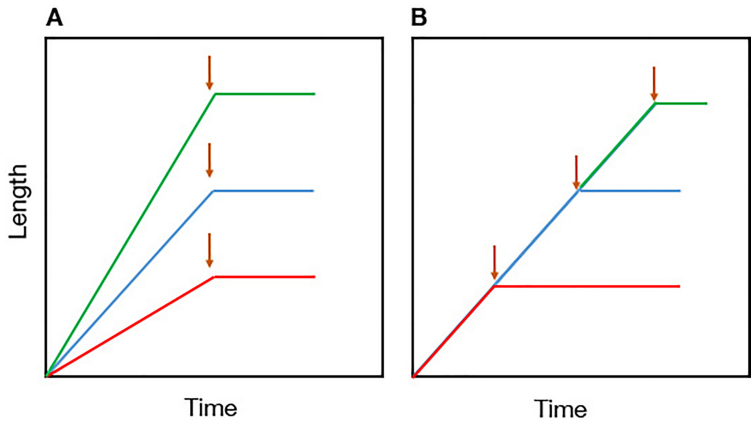

Figure 6

bioRxiv preprint doi: https://doi.org/10.1101/266759; this version posted February 16, 2018. The copyright holder for this preprint (which was not certified by peer review) is the author/funder. All rights reserved. No reuse allowed without permission.

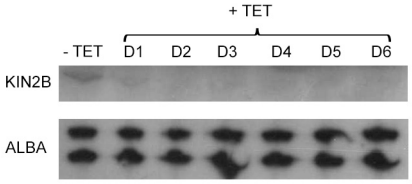

Figure S1

bioRxiv preprint doi: https://doi.org/10.1101/266759; this version posted February 16, 2018. The copyright holder for this preprint (which was not certified by peer review) is the author/funder. All rights reserved. No reuse allowed without permission.

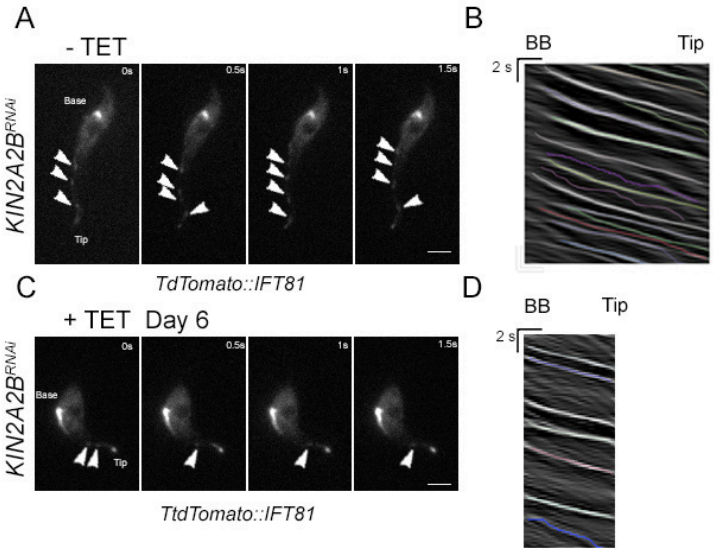

Figure S2

bioRxiv preprint doi: https://doi.org/10.1101/266759; this version posted February 16, 2018. The copyright holder for this preprint (which was not certified by peer review) is the author/funder. All rights reserved. No reuse allowed without permission.

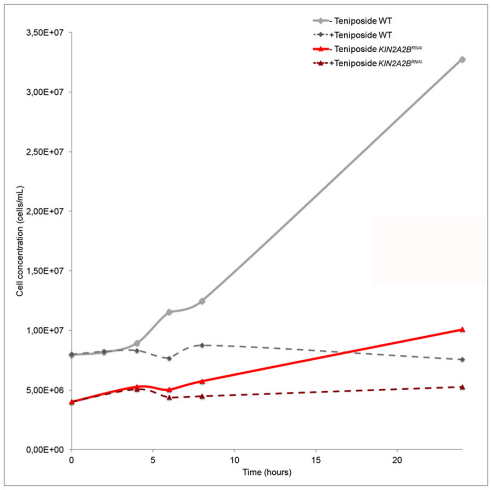

Figure S3

bioRxiv preprint doi: https://doi.org/10.1101/266759; this version posted February 16, 2018. The copyright holder for this preprint (which was not certified by peer review) is the author/funder. All rights reserved. No reuse allowed without permission.

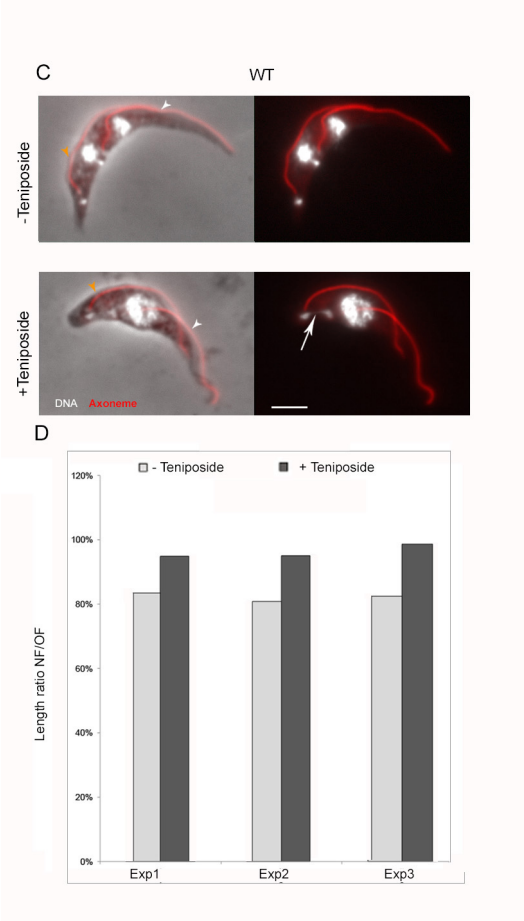

Figure S4